SANDIA REPORT

SAND98-2004
Unlimited Release
Printed September 1998

An Experimental Investigation of the Flow in a Virtual Cyclone

J. R. Torczynski, T. J. O'Hern, D. J. Rader, J. E. Brockmann, T. W. Grasser

Inside of Cover Page

SAND98-2004
Unlimited Release
Printed September 1998

An Experimental Investigation of the Flow in a Virtual Cyclone

J. R. Torczynski[1], T. J. O'Hern[1], D. J. Rader[2], J. E. Brockmann[1], T. W. Grasser[1]
[1]Engineering Sciences Center
[2]Combustion and Physical Sciences Center
Sandia National Laboratories
P. O. Box 5800
Albuquerque, New Mexico 87185-0834

Abstract

An experimental investigation has confirmed the predicted flow pattern in a prototype virtual cyclone, a novel device for nonimpact particle separation proposed by Torczynski and Rader (1996, 1997) based solely on computational simulations. The virtual cyclone differs from an ordinary cyclone in that the flow is turned by a "virtual wall" composed of an eddy rather than by a solid wall. A small-scale version of the computationally simulated geometry has been fabricated out of Lucite. The working fluid is ambient air, which is drawn through the apparatus and flow-metering equipment using a wind-tunnel vacuum source. The flow is seeded with smoke or water droplets produced by a nebulizer so that flow visualization techniques and particle-imaging velocimetry could be applied. Experiments have been performed on this apparatus for flows with Reynolds numbers from 200 up to 40,000 (a Mach number of 0.3). Flow visualization using a laser light sheet passing through the mid-plane of the apparatus verified that the computationally predicted flow is obtained over the entire range of flow rates. The shear layer between the main and recirculating flow is observed to become turbulent around a Reynolds number of 4000. While not changing the flow structure, the turbulent mixing produced by shear-layer roll-up limits particle concentration at the higher flow rates. In order to achieve highly efficient particle separation using a virtual cyclone, turbulence must be suppressed or mitigated. If laminar flow cannot be achieved for macroscopic-scale virtual cyclones, it should be achievable for a small-scale (low Reynolds number) virtual cyclone fabricated using MEMS-related technologies. This approach could lead to a chip-scale particle concentrator.

Acknowledgment

The authors particularly thank Dr. Gerold Yonas of Sandia National Laboratories for making it possible to perform this study by providing funding from the Systems, Science, and Technology Division royalty distribution revenue. The authors gratefully acknowledge Mr. Rocky J. Erven of Sandia National Laboratories who operated the High Altitude Chamber vacuum sphere to produce the flow in the experimental apparatus.

Table of Contents

List of Figures

List of Tables

Nomenclature

a	sound speed of air at ambient conditions
B	height of virtual cyclone chamber
c	particle concentration in the main flow
c_c	particle concentration in the chamber
$\tilde{c}_D$	drag coefficient of a sphere normalized to unity at zero Reynolds number
D_p	diameter of particle
D_{50}	diameter of particle of density 1 g/cm^3 at which separation efficiency is 50%
H	inlet width of virtual cyclone
L	lateral width in third dimension of virtual cyclone, normal to calculation plane
$M = U/a$	Mach number of inlet flow
p	pressure of air at ambient conditions
p_c	pressure in virtual cyclone chamber
R_1	radius of virtual cyclone inner (real) wall
$R_2 = R_1 + H$	radius of virtual cyclone outer (virtual) wall
$Re = 2\rho U H/\mu$	Reynolds number of inlet flow
T	temperature of air at ambient conditions
$t_c = V_c/\dot{V}_c$	residence time of fluid in virtual cyclone chamber
$U = \dot{V}/LH$	velocity in inlet of virtual cyclone
U_c	speed with a particular region of the virtual cyclone chamber
V	normalized terminal velocity
V_c	volume of virtual cyclone chamber
$\dot{V} = \dot{V}_s\rho_s/\rho$	volumetric flow rate of air in the main flow at ambient conditions
$\dot{V}_c$	volumetric flow rate exchanged between main and chamber flows
$\dot{V}_s$	volumetric flow rate of air in the main flow at standard conditions
W	outlet width of virtual cyclone
η	particle-separation efficiency
θ	angle through which the main flow is turned
μ	absolute viscosity of air at ambient conditions
ρ	density of air at ambient conditions
ρ_p	density of particle
ρ_s	density of air at standard conditions (21 ˚C and 101,325 Pa, 1.200 kg/m^3)

cfm	cubic feet per minute
lpm	liters per minute
slpm	standard liters per minute (equivalent flow rate at 21 ˚C and 101,325 Pa)

1. Introduction

1.1. Overview

An experimental investigation has confirmed the predicted flow pattern in a prototype virtual cyclone, a novel device for nonimpact particle separation proposed by Torczynski and Rader (1996, 1997) based solely on computational simulations. The virtual cyclone differs from an ordinary cyclone in that the flow is turned by a "virtual wall" composed of an eddy rather than by a solid wall. A small-scale version of the computationally simulated geometry has been fabricated out of Lucite. The working fluid is ambient air, which is drawn through the apparatus and flow-metering equipment using a wind-tunnel vacuum source. The flow is seeded with smoke or water droplets produced by a nebulizer so that flow visualization techniques and particle-imaging velocimetry could be applied. Experiments have been performed on this apparatus for flows with Reynolds numbers from 200 up to 40,000 (a Mach number of 0.3). Flow visualization using a laser light sheet passing through the mid-plane of the apparatus verified that the computationally predicted flow is obtained over the entire range of flow rates. The shear layer between the main and recirculating flow is observed to become turbulent around a Reynolds number of 4000. While not changing the flow structure, the turbulent mixing produced by shear-layer roll-up limits particle concentration at the higher flow rates. In order to achieve highly efficient particle separation using a virtual cyclone, turbulence must be suppressed or mitigated. If laminar flow cannot be achieved for macroscopic-scale virtual cyclones, it should be achievable for a small-scale (low Reynolds number) virtual cyclone fabricated using MEMS-related technologies. This approach could lead to a chip-scale particle concentrator.

1.2. Motivation

It is desirable under certain circumstances to separate particles from a flow stream without the particles coming in contact with a solid surface. This can occur if the particle-surface contact would modify either particle or surface properties in an undesirable manner. Examples include separating fractal-like chain agglomerates, the morphology of which could be modified substantially by impact onto a solid surface.

In a similar fashion, it is sometimes desirable to increase the particle concentration of a particle-laden flow stream. This minimizes the amount of the fluid containing the particles and also can improve the possibility of characterizing particle properties. Examples include concentrating liquid suspensions of radioactive waste for disposal purposes and concentrating airborne particles for improved characterization.

In some situations, it is desirable to separate the particles from large volumes of particle-laden fluid without using large amounts of power or energy. To achieve this, a system must be developed that is capable of high flow rates with low pressure drops. Examples include industrial air cleaning systems.

Torczynski and Rader (1996, 1997) presented a concept called the "virtual cyclone" (the original term "anticyclone" was changed to parallel the term "virtual impactor"), which has the potential to meet each of these requirements. However, their investigation involved only computer simulations: no experiments were performed to verify the concept. Since many "real life" factors not accounted for in the computational model could significantly affect the behavior and performance of a virtual cyclone (e.g., turbulence details, three-dimensionality, transient phenomena, particle-turbulence interaction), it is essential that a proof-of-principle experiment be performed to demonstrate the basic concept and to indicate possible improvements.

1.3. The Virtual Cyclone Concept

The basic concept of a virtual cyclone was first presented by Torczynski and Rader (1996, 1997). This concept was originally called the “anticyclone” but was subsequently renamed the “virtual cyclone” to maintain consistency with the well established terms “impactor” and “virtual impactor”. The term “virtual cyclone” is also more descriptive of the predicted flow pattern, shown in Figure 1. In this concept, a particle-laden flow enters a chamber through a long, thin inlet. On one side of the inlet, the wall curves away from the main flow direction. Unlike a conventional cyclone, there is no wall that curves into the main flow direction. Rather, an eddy forms in the chamber and serves as a “virtual wall” to turn the main flow. Particles carried in the main stream cannot turn as rapidly as the flow and are transferred from the main flow to the eddy flow. This transfer from one flow stream to another without impacting a solid wall is “nonimpact” particle separation. In the case of a confined eddy, the possibility exists of achieving particle concentrations within the eddy that are much larger than in the main flow stream.

Torczynski and Rader (1996, 1997) used the computational fluid dynamics code FIDAP (Fluid Dynamics International, 1993) to study a particular virtual-cyclone geometry, shown in Figure 2. Their simulations showed that the basic flow pattern reproduced in Figure 2 is obtained robustly over (at least) four orders of magnitude of flow rate and is not strongly affected by turbulence. More specifically, they found that the basic flow pattern in Figure 1 is obtained in the geometry of Figure 2 so long as the Reynolds number is at least 100, with the Reynolds number Re defined to be

$$Re = \frac{\rho U(2H)}{\mu}, \tag{1}$$

where H and U are the inlet width and the average flow speed in the inlet, respectively. They also developed an approximate implicit relationship for the particle-separation efficiency η in terms of the Stokes number St and particle Reynolds number Re_p:

$$St = \frac{\rho_p D_p^2 U}{18\mu R_1}, \tag{2}$$

$$Re_p = \frac{\rho U D_p}{\mu}, \tag{3}$$

$\tilde{c}_D V = (R_1/R_2)St$, where $\tilde{c}_D$ is a function of the radial Reynolds number $Re_p V$, (4)

$$\eta = \left(\frac{R_2}{R_2 - R_1}\right)\left\{1 - [\cosh(\theta/V)]^{(-V^2)}\right\} \approx \frac{\rho_p D_p^2 U\theta}{18\mu H}, \quad \eta = \min(1, \eta), \tag{5}$$

where V is the radial terminal velocity normalized by the inlet velocity U, θ is the angle through which the main flow is turned (typically around $\pi/2$), and $\tilde{c}_D$ is the drag coefficient normalized to unity at $Re_p V = 0$. After specification of geometric, flow, and particle parameters, Equation 4 is solved iteratively to find V using a model for the particle drag coefficient such as $\tilde{c}_D \approx 1$ or the more accurate model of Turton and Levenspiel (1986). Equation 5 then yields the efficiency η. All of these results are obtained for Mach numbers M small compared to unity where a is the sound speed:

$$M = \frac{U}{a} \ll 1. \tag{6}$$

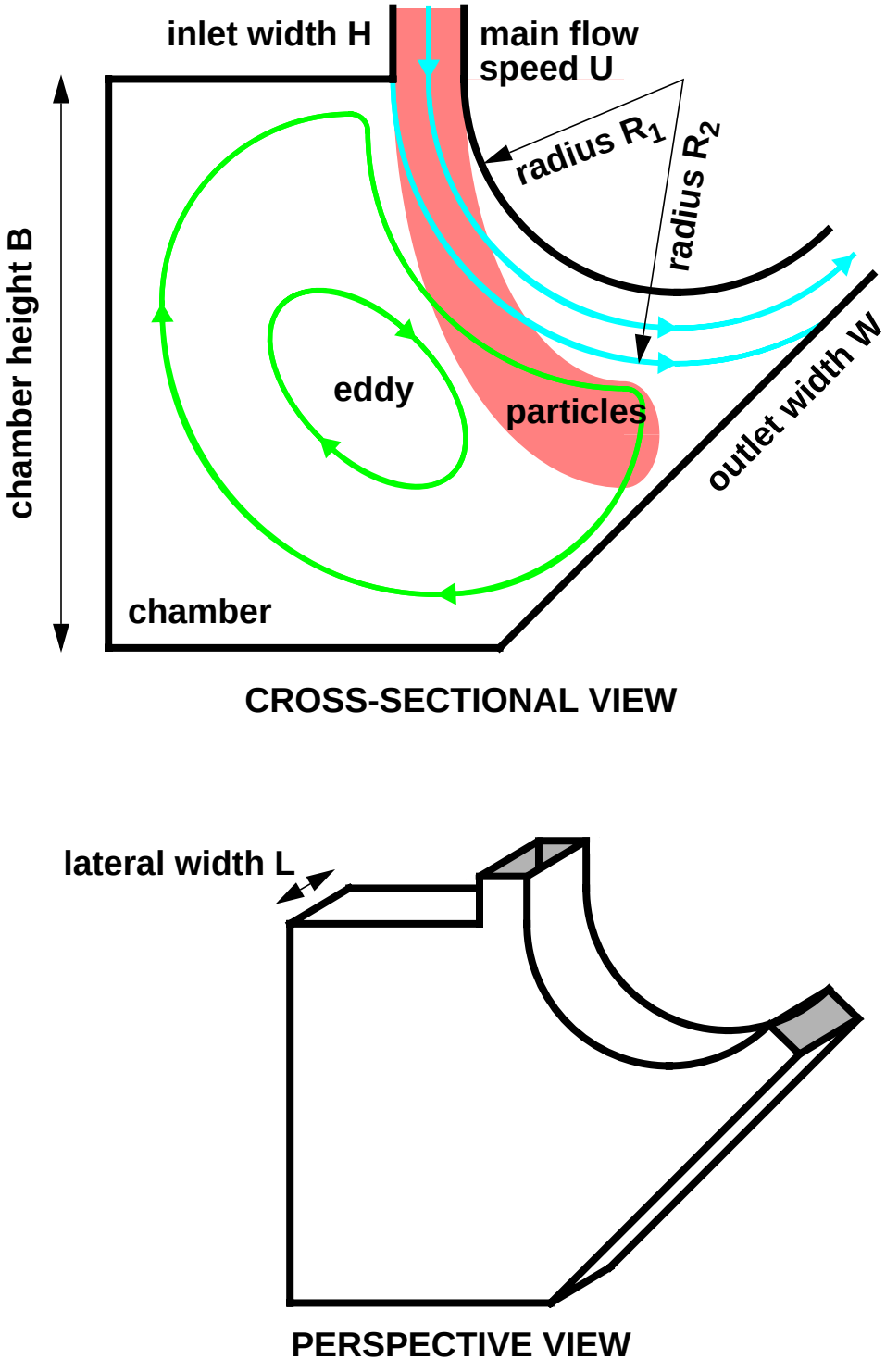

Figure 1. The virtual cyclone: schematic diagrams after Torczynski and Rader (1997).

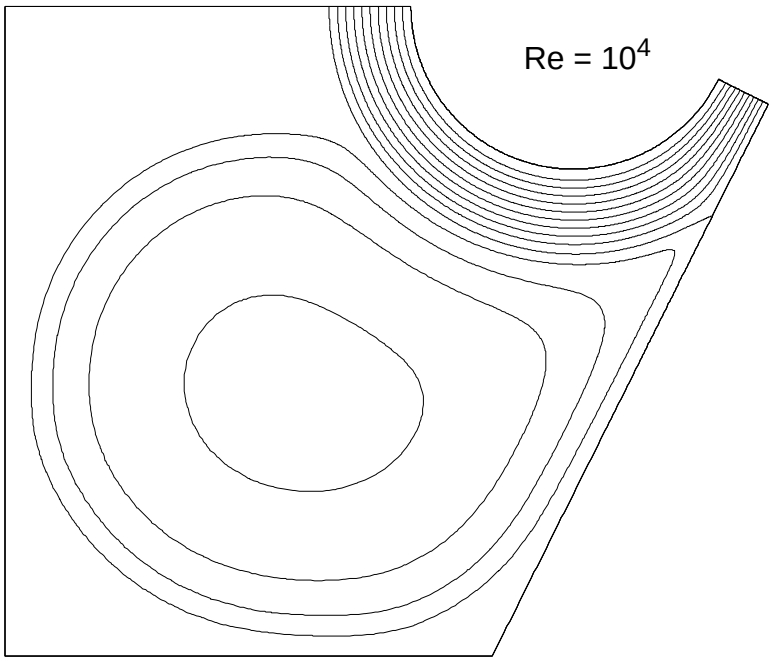

streamlines

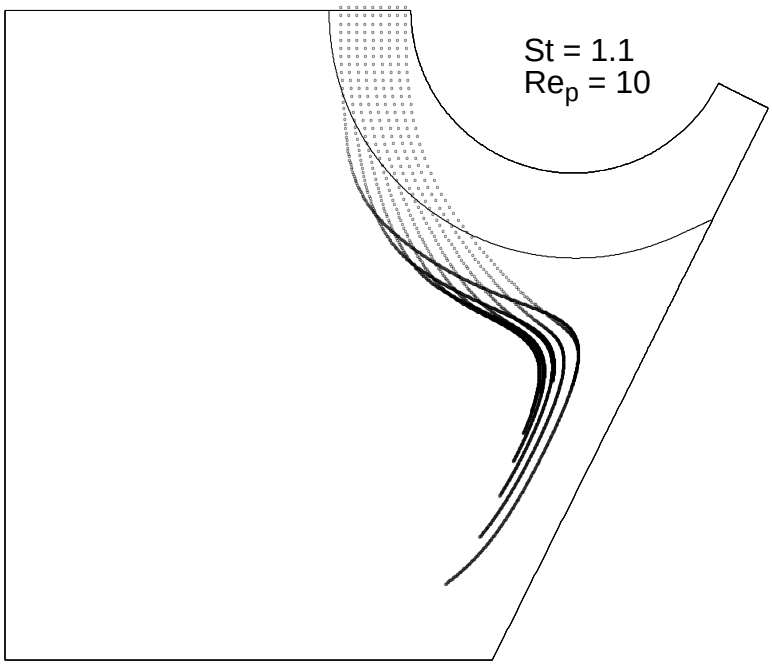

particle paths

Figure 2. The virtual cyclone: computational example from Torczynski and Rader (1997).

2. Virtual Cyclone Experimental Apparatus

2.1. Overview

In this section, the virtual cyclone experimental apparatus is described. More specifically, the prototype virtual cyclone and the flow system to which it is connected are discussed.

2.2. Prototype Virtual Cyclone

In the design of a virtual cyclone, there are many geometric parameters that must be specified. For example, the shape of the chamber in which the eddy resides needs to be determined (see Figure 1). To enable a direct comparison to the study of Torczynski and Rader (1996, 1997), a prototype virtual cyclone has been constructed that is geometrically similar to the one they modeled. In their study, they did not claim that this is an optimal design; nevertheless, their simulations indicated that this geometry should exhibit the virtual-cyclone flow pattern shown in Figure 1. Once similarity is enforced, there remains only one in-plane length parameter to be selected (e.g., the inlet width H). The out-of-plane lateral length L must also be selected. To avoid a strongly three-dimensional flow, it should be sufficiently larger than any in-plane length. Table 1 delineates the values selected for the geometric parameters shown in Figure 1, Figures 3 and 4 show drawings of the apparatus, and Figure 5 shows two photographs of the completed apparatus.

Table 1. Geometric parameter values of prototype virtual cyclone.

Quantity	Symbol	Value
Inlet width	H	0.125 inch
Outlet width	W	0.090 inch
Inner radius	R_1	0.250 inch
Outer radius	R_2	0.375 inch
Chamber height	B	1.00 inch
Lateral length	L	3.0 inch
Turning angle	θ	$\pi/2 = 90°$

The prototype virtual cyclone shown in these figures is fabricated out of Lucite pieces that are chemically bonded together between two side disks to form an airtight structure. In an attempt to mitigate the influence of room-air motion on the flow in the virtual cyclone, the side disks are chosen to be fairly large: 12 inches in diameter compared to a chamber height of 1 inch (see Figures 3-4). Also, all sharp edges upstream of the inlet are rounded off to reduce the likelihood of turbulent flow occurring upstream of the inlet. Thus, the flow approaching the inlet can be described as cylindrically converging. The lateral length L, which specifies the separation between the side disks, is selected to be 3 inches, an intermediate value between the in-plane chamber length scales of around 1 inch and the side disk radius of 6 inches. These choices produce an inlet with an aspect ratio of 24:1. The flow from the virtual cyclone outlet travels along a gently expanding diffuser and enters a roughly cubical box that is connected to the flow system.

Table 2 shows the properties of air at ambient conditions, and Table 3 shows flow and particle-separation properties for the accessible range of flow rates based on the values in Tables 1-2. The chamber pressure p_c is estimated using the incompressible Bernoulli relation, which is restricted to modest values of the Mach number (say, $M \leq 0.3$):

$$p - p_c \approx \rho U^2/2, \tag{7}$$

where p and ρ are the pressure and density of air at ambient conditions, and U is the speed of the flow as it passes through the inlet. Particle separation is quantified in terms of D_{50}, the diameter of a particle having a density ρ_p of 1 g/cm^3 for which a 50% separation efficiency is achieved ($\eta = 1/2$):

$$\eta \approx \frac{\rho_p D_{50}^2 U \theta}{18 \mu H} = \frac{1}{2}, \text{ for } \tilde{c}_D \approx 1. \tag{8}$$

Table 2. Properties of air at ambient conditions.

Quantity	Symbol	Value
Pressure	p	84,100 Pa = 12.2 psi
Temperature	T	294 K = 21 ˚C
Density	ρ	1.00 kg/m^3
Absolute Viscosity	μ	1.83×10^{-5} kg/(m·s)
Sound Speed	a	344 m/s

Table 3. Flow and particle-separation properties of the prototype virtual cyclone.

U (m/s)	$\dot{V}$ (lpm [cfm])	Re	M	$p - p_c$ (Pa [psi])	D_{50} (μm)	Re_p at D_{50}
1	14.5 [0.512]	347	0.0029	0.5 [0.000073]	18	1.0
3	43.5 [1.54]	1,040	0.0087	4.5 [0.00065]	11	1.7
10	145 [5.12]	3,470	0.029	50 [0.0073]	5.8	3.2
30	435 [15.4]	10,400	0.087	450 [0.065]	3.3	5.5
100	1,450 [51.2]	34,700	0.29	5000 [0.73]	1.8	10

Several observations can be made about these values. First, for velocities in the range of 1-100 m/s, particles with diameters of roughly 2-20 μm can be separated. Second, particle Reynolds numbers are modest when evaluated at D_{50}. Third, even at the high end of the velocity range, the Mach number is low enough for the incompressible assumption to be reasonable. Fourth, since turbulence often occurs for Reynolds numbers exceeding a few thousand, experiments at the higher velocities may be turbulent. Fifth, pressure drops are modest for all but the highest flow rates.

all dimensions in inches

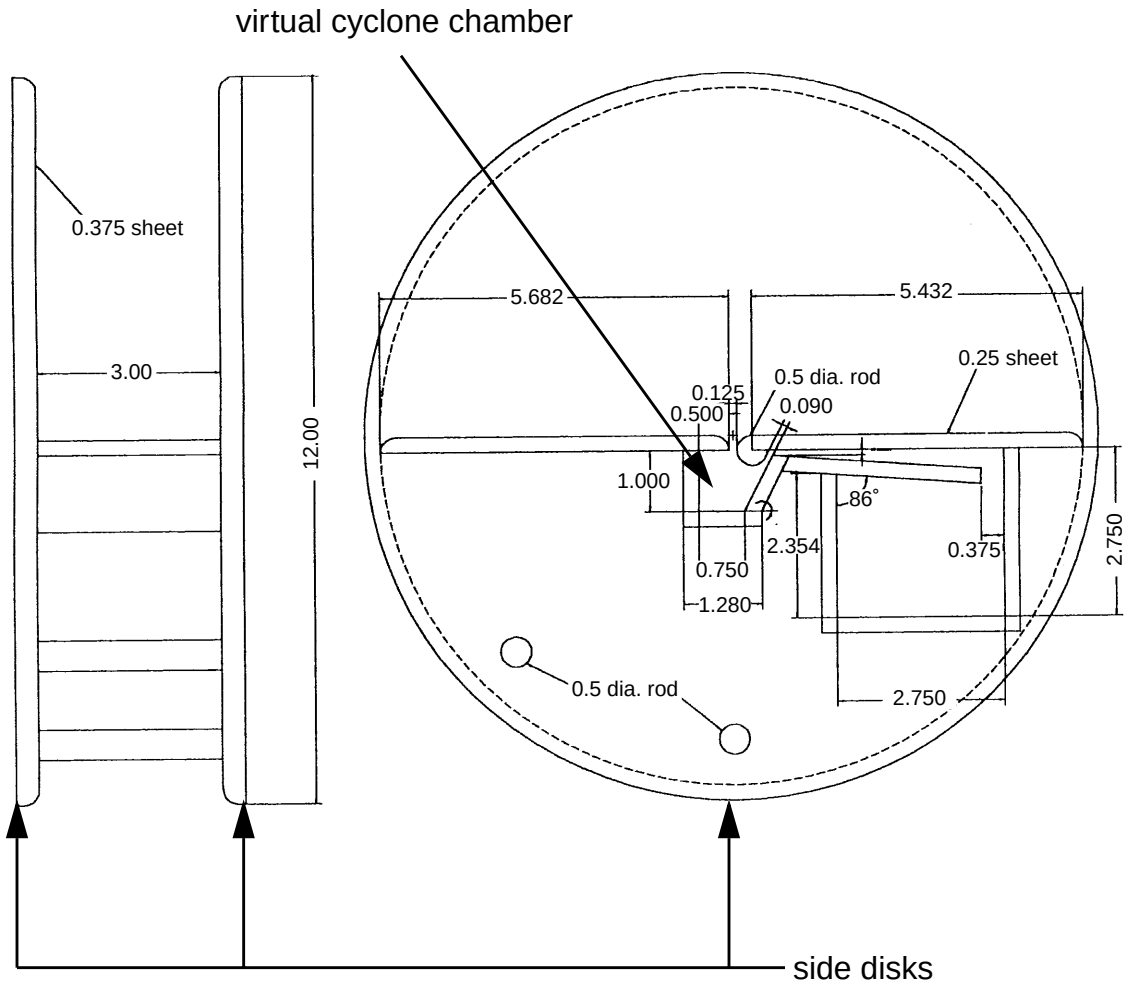

Figure 3. Diagram of prototype virtual cyclone apparatus: full view.

all dimensions in inches

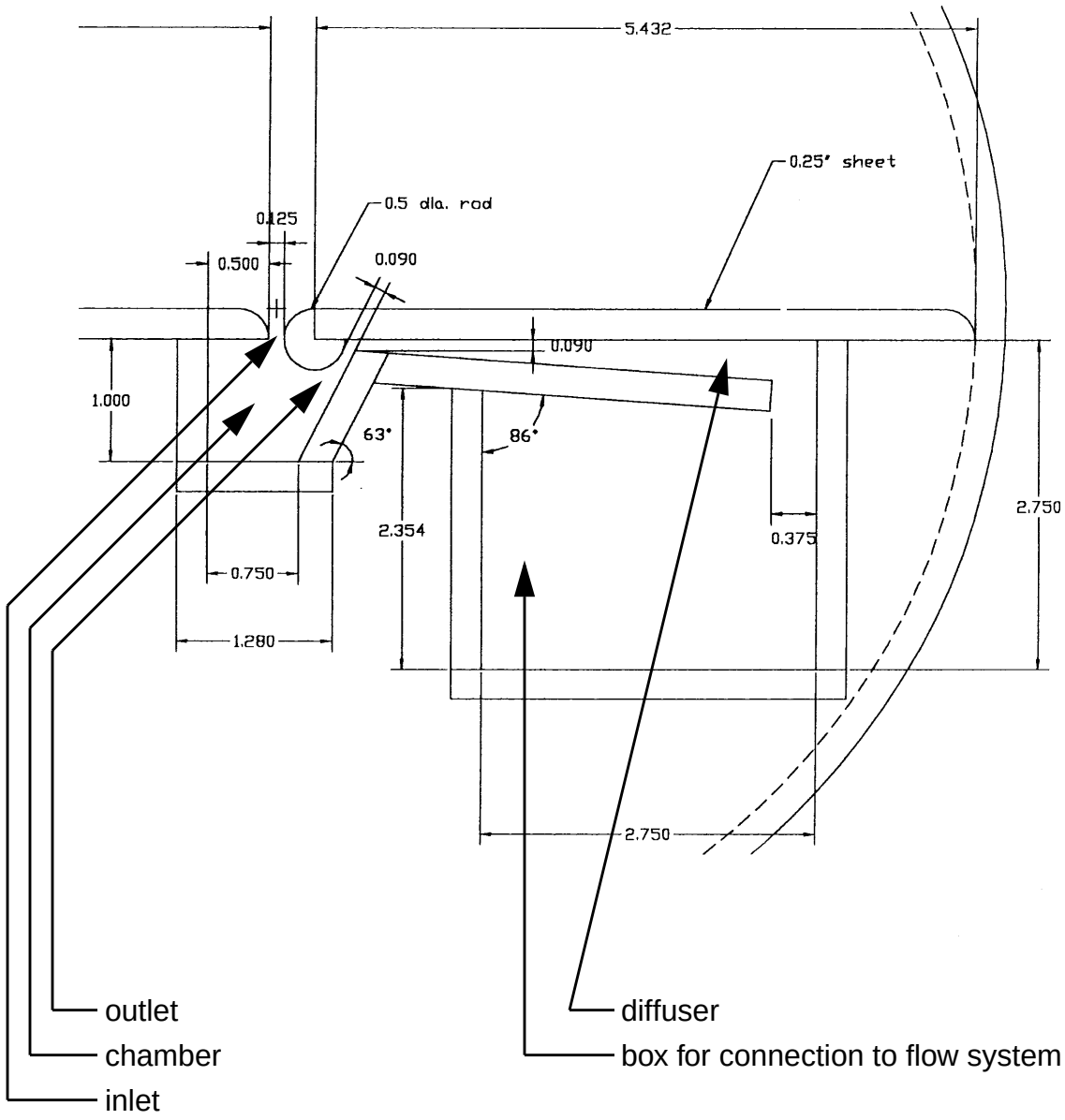

Figure 4. Diagram of prototype virtual cyclone apparatus: chamber details.

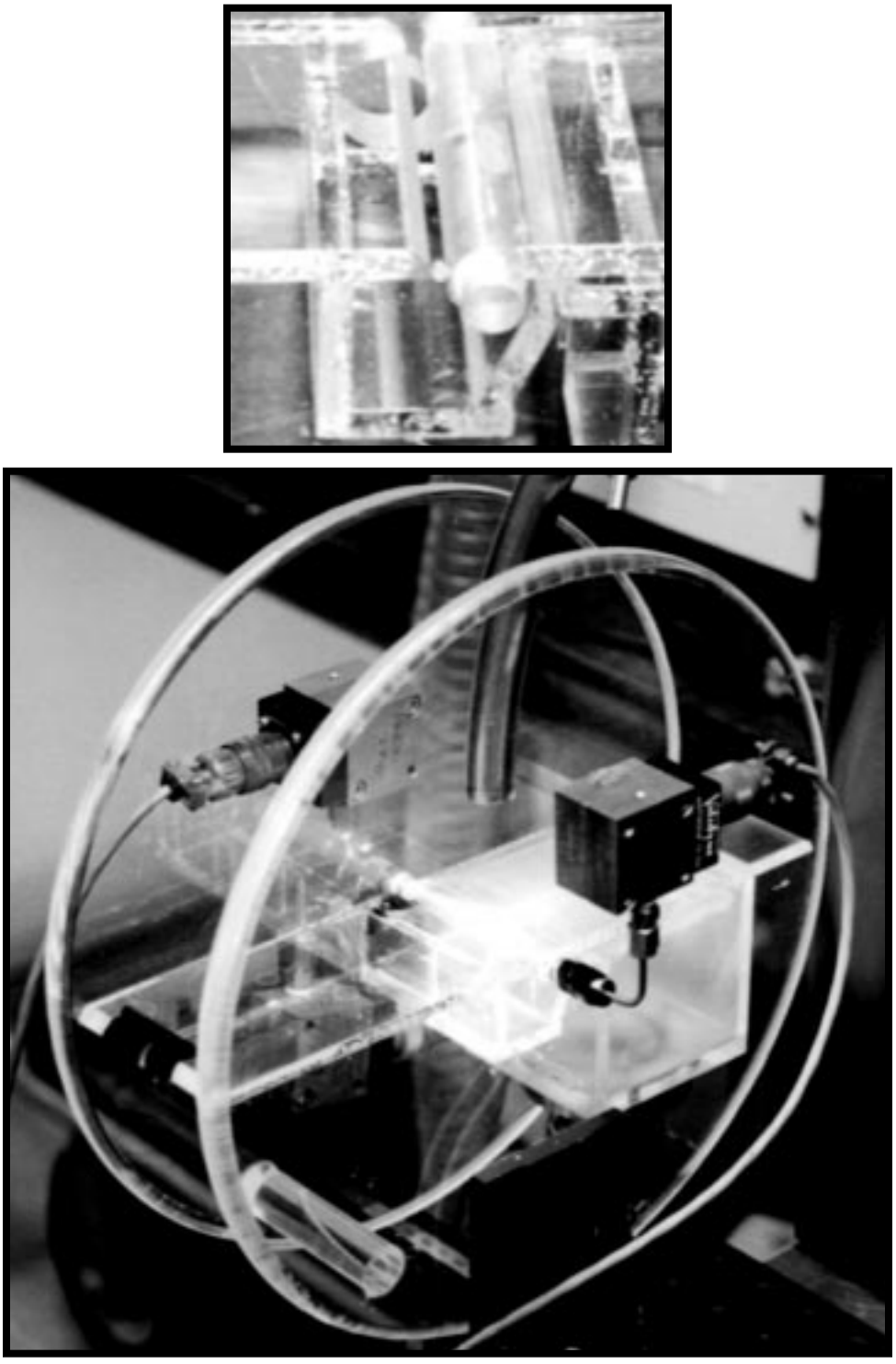

Figure 5. Photographs of prototype virtual cyclone.

2.3. Flow System

The flow system used to draw air through the prototype virtual cyclone is shown in Figure 6 and operates as follows. Ambient room air is the working fluid. It is drawn into the space between the virtual cyclone side disks, through the inlet, out the outlet, and into the box connecting the virtual cyclone to the remainder of the flow system. The air travels down a roughly 10-ft length of 1.5-inch-ID steel-coil-reinforced flexible vacuum hose to a HEPA filter, which removes any particles from the flow. The air then passes through a mass flow meter, down a further length of the flexible vacuum hose, and through two throttling valves, which control the flow rate, before being exhausted into the large-diameter line connecting to a large evacuated spherical vessel outside the building. This vacuum sphere, Sandia's High Altitude Chamber (HAC) facility, has a 27-ft diameter and an internal volume of approximately 10,000 ft^3 and is one of three such vessels. During use, the pressure within the HAC is maintained at the prescribed near-vacuum value by continuous pumping.

A Matheson Mass Flow Meter (Model 8104-1416-FM) is used to measure the mass flow rate and is shown in Figure 7. In this meter, a small obstruction in the main flow channel produces a pressure difference that drives a flow through a small side channel paralleling the main channel. A prescribed heating rate is applied to the side channel, and the resulting temperature rise is correlated to the mass flow rate. The output of this meter is the volume flow rate $\dot{V}_s$ in standard liters per minute (slpm). To find the volume flow rate $\dot{V}$ at ambient conditions, the following relation is used:

$$\dot{V} = \dot{V}_s\left(\frac{\rho_s}{\rho}\right), \tag{9}$$

where ρ_s and ρ are the standard air density (at 21 ˚C and 101,325 Pa: 1.200 kg/m^3) and the air density at ambient conditions, respectively. Under ordinary experimental conditions, the density ratio is found to be $\rho_s/\rho = 1.2$. The output of this meter is a percentage of the maximum allowable flow rate, 1500 slpm.

Pressure is measured at several locations in the system. Three Validyne pressure gauges (Model DP 15-36, with a 20-psi range) are attached to the virtual cyclone as shown in Figure 8. These gauges are used to measure the pressures at the inlet, at the outlet, and in the center of the chamber. An additional pressure gauge and a Type K thermocouple are mounted just upstream of the mass flow meter so that the flow conditions entering the meter are known. Even at the highest flow rates (90% of the full range of the Matheson), the temperature at this location remains above 15 ˚C, which is not much lower than the ambient temperature of 21 ˚C.

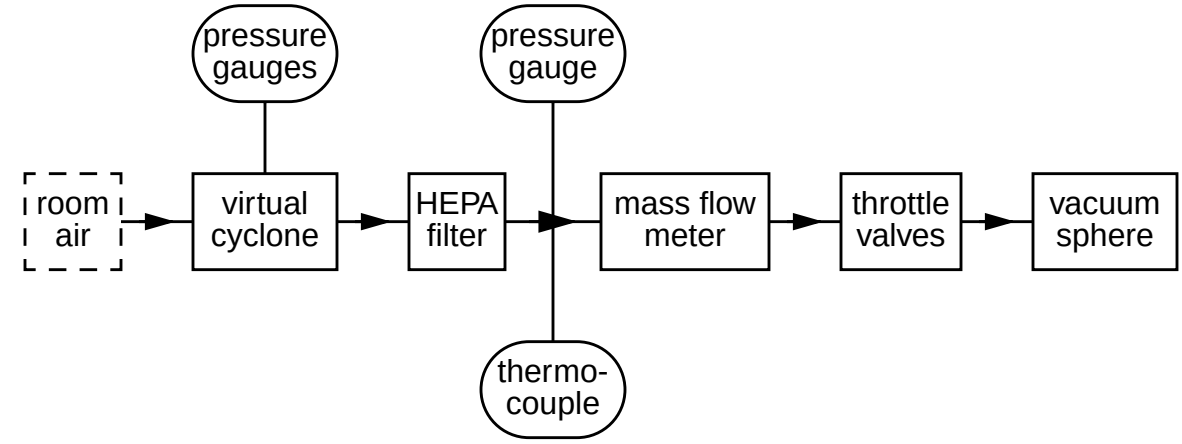

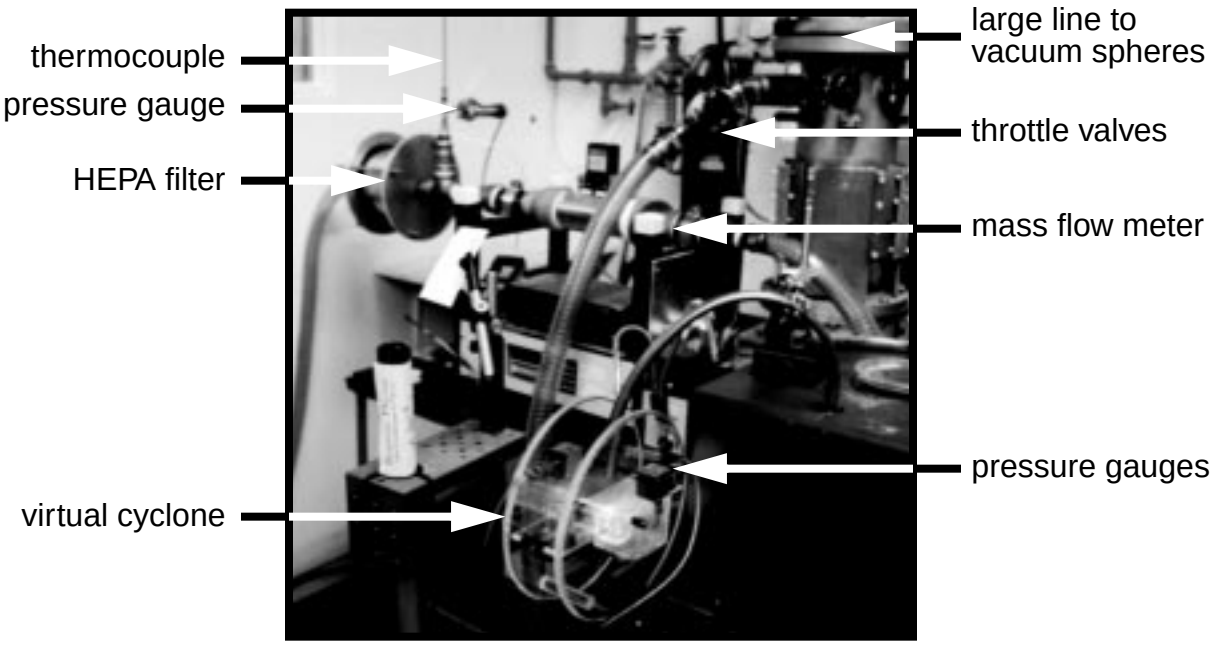

Figure 6. Schematic diagram and photograph of the flow system.

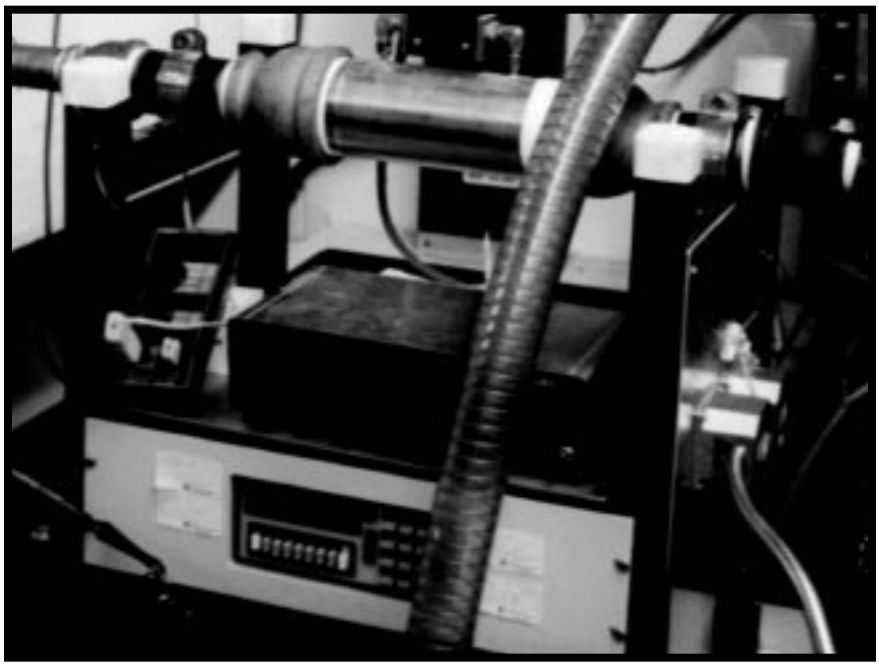

Figure 7. Photograph of the Matheson mass flow meter.

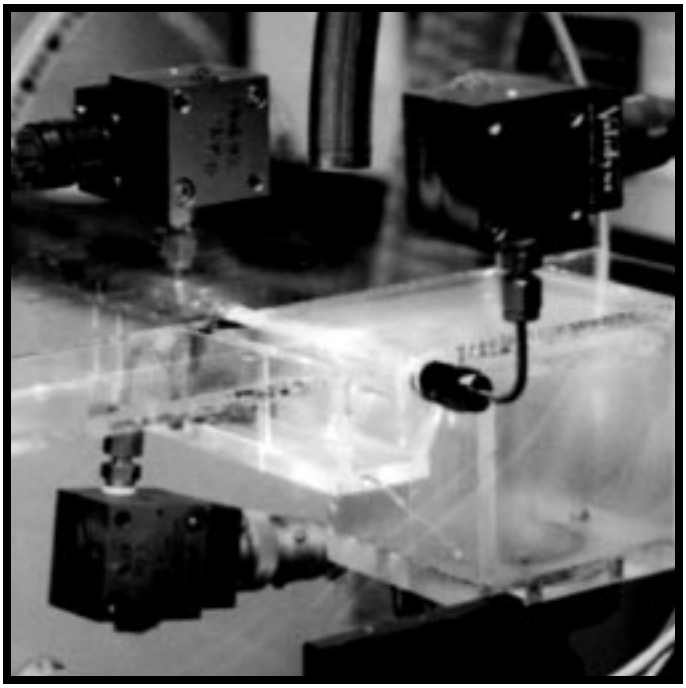

Figure 8. Photograph of the pressure transducers (installed).

3. Flow Diagnostic Techniques

3.1. Overview

In this section, the techniques used to perform flow visualization and particle-imaging velocimetry (PIV) experiments are described. These include the system used to produce the laser light sheet for illuminating the flow, the particle-dispersion techniques for seeding the flow, and the image-recording techniques (still photography and standard VHS video).

3.2. Laser Light Sheet

All flow experiments are performed using a laser light sheet for illumination. The laser light sheet is approximately 1 mm in thickness and passes through the symmetry plane of the virtual cyclone (the plane equidistant from the two side disks). This light sheet is produced using one or two Coherent Infinity 40-100 lasers, which are frequency-doubled Nd:YAG lasers with an output wavelength of 532 nm. These lasers are Q-switched and produce 8-ns pulses containing 15-20 mJ (in the IR) at pulse rates up to 100 Hz. Since the pulse duration is extremely short compared to the time scales of motion, a long-exposure photograph records a succession of images that indicate a particle's position at successive intervals of 0.01 s.

Although the 0.01-s time separation between successive laser pulses seems small, it is actually too long for quantitative velocity measurements to be made at all but the slowest velocities. For larger velocities, two lasers of the type describe above are pulsed sequentially with a prescribed separation between the two pulses, which is referred to as the "double-pulse" method of operation. A separation between particle images of about 1 mm is desirable for velocity calculations, so the product of the flow speed with the pulse separation should be about 1 mm. Thus, a pulse separation of around 10 μs should be used for a flow speed of 100 m/s.

3.3. Particle-Seeding Techniques

Laser-light-sheet experiments require particles to be introduced into the flow so that their positions can be tracked to determine the fluid motion. Two particle-seeding techniques are applied: nebulization of water droplets and dispersion of dry powders (smoke injection was abandoned after a few early experiments). Figure 9 shows a picture of the DeVilbiss nebulizer used in these experiments. In this device, compressed air is forced over the orifice of a small tube inserted into a liquid reservoir, and the Bernoulli effect draws liquid up into the gas flow stream, in which it is atomized. The resulting dense "fog" of water droplets (3-10 μm in diameter) exits the nebulizer at a much slower velocity and is easily observed with the laser light sheet. The nebulizer must be positioned near the point at which particles are to be injected into the flow. Figure 10 shows a picture of the TSI Model 3433 Small Scale Powder Disperser (SSPD). In this device, a flow is used to suction off particles coated on the grooved surface of a rotating stage. The particle flux is controlled by the flow velocity and the stage rotational speed. These particles are transported to the particle-injection location through a 0.75-inch-ID curved tube. To date, two types of particles have been used in the SSPD: polymethylmethacrylate (PMMA) spheres (Bangs Laboratories, 3-11 μm in diameter) and Bermuda grass smut spores (Duke Scientific, 5.8-8.2 μm in diameter). Unfortunately, the particle delivery from the SSPD was found to be erratic for both particle types, so the laser-light-sheet experiments employed the nebulizer for particle seeding.

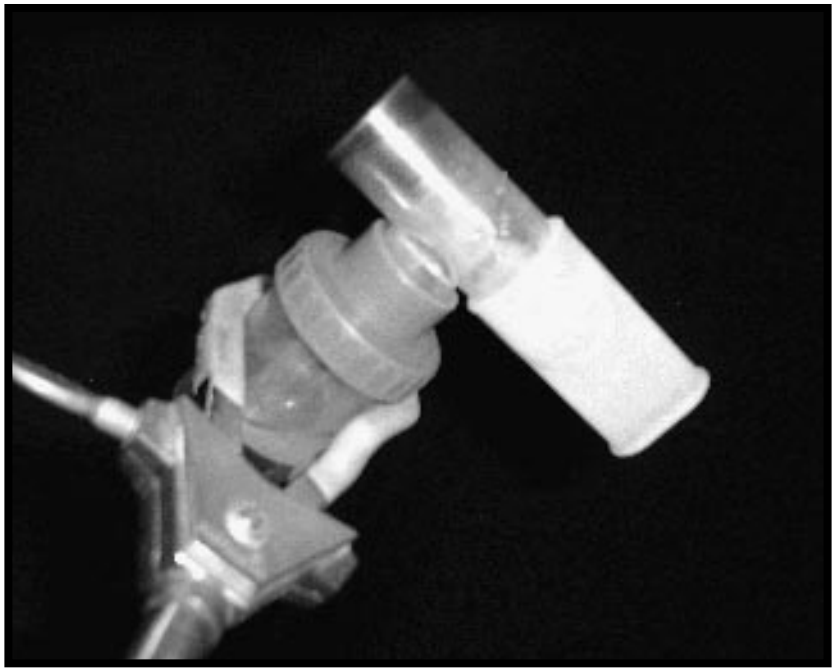

Figure 9. Photograph of the DeVilbiss nebulizer used for particle seeding.

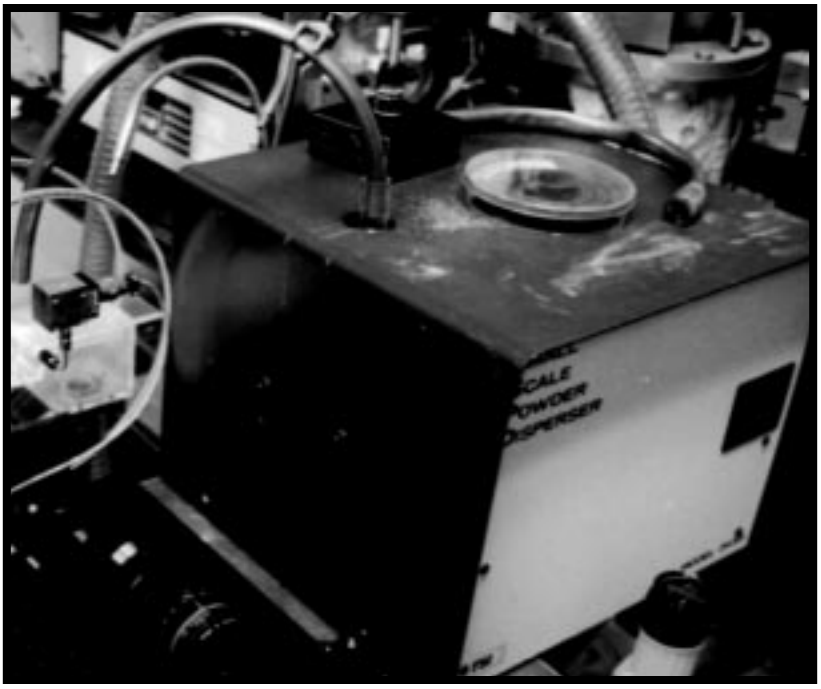

Figure 10. Photograph of the Small Scale Powder Disperser (SSPD) used for particle seeding.

3.4. Visualization Techniques

Three different techniques are employed to record images from the laser-light-sheet experiments: a standard 35-mm camera, a digital camera, and a VHS video recorder with frame-grabber software.

A Nikon N8008 camera is used to take 35-mm photographs of the flow. The light level is controlled by adjusting the power of the laser pulses, and the shutter is opened for a prescribed duration, typically 1/4, 1/8, or 1/15 s. When laser pulses are generated at a rate of 100 Hz, this technique yields 24-26, 12-13, or 6-7 pulses per frame, respectively. Due to slight out-of-plane motion of particles, the number of correlated images per particle per frame is usually somewhat less. In the double-pulse method of operating the lasers, only two correlated images per particle appear in each frame. Such pictures can be analyzed using PIV software to determine quantitative information about flow velocities.

A Fuji MX-700 digital camera is also used to obtain photographs of the flow. This camera has a resolution of 1280×1024 pixels and has the advantage of producing images in JPEG format that can be analyzed directly with standard image-processing software. Although the same types of images are recorded as with the Nikon, the images are available almost immediately since there is no film to develop. This rapid turnaround greatly facilitates data acquisition and analysis.

A Panasonic PalmSight PV-L657 camcorder is used to record VHS videos of the flow. The resulting flow-visualization video is viewed using a standard VCR. The Snappy frame-grabber software package (Play, Inc., 1998) is used to select individual frames from the video and can create files of these images in standard formats like TIF (Tagged Image Format) for further analysis. The video is particularly useful for gaining insight into important issues like flow stability and turbulence, which are difficult to investigate using only single-frame information from the Nikon and Fuji cameras.

3.5. Particle-Imaging Velocimetry (PIV)

Particle-imaging velocimetry (PIV) is a standard technique to determine velocity fields. The present implementation of this technique is described extensively elsewhere (O'Hern et al., 1997) and is implemented as follows. A flow is seeded with particles having properties that enable them to follow the flow and to be seen when illuminated with light. Successive images are compared to determine the differences in particle positions from one frame to the next, which enables the particle velocity to be determined. Typically, this comparison is made either by tracking individual particles or by using cross correlation or Fourier analysis on small portions of each frame. The result is a map of velocity vectors of the portion of the flow containing enough particles to achieve a reasonable correlation between successive frames.

4. Experimental Results

4.1. Overview

In this section, results are presented for several series of flow experiments in the prototype virtual cyclone. These results include chamber pressure as a function of flow rate, standard and digital flow-visualization photographs with the nebulizer in different positions, and frames taken from the video, which are chosen to illustrate certain physical phenomena.

4.2. Flow Conditions

As discussed in a previous section, the pressure difference $p - p_c$ from ambient conditions to the chamber interior can be estimated from the inlet velocity U and the gas density ρ by applying the Bernoulli relation:

$$p - p_c \approx \rho U^2 / 2 . \tag{10}$$

The inlet velocity is determined from the inlet dimensions and the volume flow rate:

$$U = \left(\frac{\dot{V}_s}{HL}\right)\left(\frac{\rho_s}{\rho}\right). \tag{11}$$

Table 4 shows a comparison of the measured and predicted pressure differences over the accessible range of flow rates. The agreement between the measured and predicted values is acceptable given the uncertainty in the inlet width H (+0%, -10%) and the approximations underlying the model (e.g., incompressible flow, $M \ll 1$, uniform inlet velocity).

Table 4. Chamber flow conditions over the operating range (ambient is 12.2 psi, 21 ˚C).

Meter (%)	$\dot{V}_s$ (slpm)	U (m/s)	Re	M	$p - p_c$ meas. (psi)	$p - p_c$ pred. (psi)
0.5	7.5	0.62	215	0.0018	n/a	0.00
1	15	1.24	430	0.0036	0.00	0.00
3	45	3.72	1,290	0.011	n/a	0.00
10	150	12.4	4,300	0.036	0.01	0.01
25	375	31.0	10,750	0.090	0.08	0.07
30	450	37.2	12,900	0.11	n/a	0.10
50	750	62.0	21,500	0.18	0.30	0.28
75	1125	93.0	32,250	0.27	0.72	0.63
90	1350	112.	38,700	0.32	1.05	0.91
100	1500	124.	43,000	0.36	n/a	1.12

4.3. Flow Visualization Results

Figures 11-19 show images of the flow in the prototype virtual cyclone for a variety of flow rates, particle types, particle-injection locations, and illumination types. The flow rate is specified in terms of the percentage of the full range of the Matheson mass flow meter. Table 4 enables this value to be directly converted into a wide variety of physical quantities, such as volume flow rate at standard conditions, inlet velocity, Reynolds number, and Mach number. Two types of particles are employed: smoke and water droplets from a nebulizer. The former is difficult to control and is used only in Figure 11. The latter is more straightforward (although water can build up on the chamber surfaces) and is used in the remainder of the figures. Two locations are employed for particle injection: back-plane injection, in which the particle source is placed as near to the back side disk as possible (out of the plane of laser illumination), and mid-plane injection, in which the particle source is placed equidistant between the two side disks (in the plane of laser illumination). Due to lateral transport of particles in the eddy, back-plane injection enables the eddy to be visualized while keeping the main flow clear of particles. Two types of illumination are employed: 8-ns laser pulses produced at a rate of 100 Hz, referred to as “100-Hz”, and two 8-ns laser pulses with a prescribed separation, referred to as “double-pulse”. Figure captions containing a pulse separation (e.g., 0.5 ms) rather than the “100 Hz” designator, are double-pulse photographs using the indicated pulse separation.

Figure 11 shows the flow pattern observed in the prototype virtual cyclone using smoke visualization at a flow rate around 1% with 100-Hz illumination. The smoke is injected along the back-plane (out of the plane of laser illumination) in the top photograph, whereas smoke is injected along the mid-plane (in the plane of laser illumination) in the bottom photograph. The predicted virtual-cyclone flow pattern is clearly visible for both particle-injection locations. The main flow (see Figure 1) is seen to be devoid of particles in the case of back-plane injection, whereas the streamlines in the main flow are easily visible in the case of mid-plane injection. In both cases, the eddy is filled with smoke. The “ripples” in the eddy regions of both pictures result from the fact that the illumination is pulsed (essentially stroboscopic) rather than continuous. Since the illumination occurs at 100 Hz, the spacings between adjacent ripples can be used to determine the velocity at ripple locations.

Figure 12 contains two video frames that illustrate the impact of the nebulizer on the flow in the chamber at zero flow rate. The top frame shows the quiescent case of zero main flow and the nebulizer turned off. No particles are observed in the chamber. The bottom frame shows what occurs when the nebulizer is turned on with zero main flow. As the nebulizer is turned on, it produces a turbulent jet between the side disks. The large-scale structures (turbulent eddies) in this jet impinge on the inlet and produce vortex-line pairs (the two-dimensional analog to vortex ring) traveling downward in the chamber. This suggests that the nebulizer can disturb the virtual cyclone flow pattern at low flow rates. Similar flow disturbances in the chamber are seen when the laboratory ventilation is turned on, so care is taken to operate the virtual cyclone only when the laboratory ventilation is off.

Figure 13 illustrates the difference between double-pulse and 100-Hz illumination at a flow rate of 0.5%. The top photograph employs mid-plane particle injection and 100-Hz illumination, whereas the bottom photograph employs back-plane particle injection and double-pulse illumination with a pulse separation of 20 ms. The basic virtual cyclone flow pattern is clearly visible in both cases, suggesting that the main flow is fairly insensitive to disturbances from the nebulizer at low flow rates. However, the nebulizer is seen to disturb the flow somewhat in the eddy region at this low flow rate, especially for the case of back-plane particle injection. These disturbances are not as readily apparent in the longer-exposure photographs with 100-Hz illumination. It is conjectured that they represent puffs of particles resulting from the turbulent eddies in the nebulizer jet and that these puffs are passively convected around the chamber.

Figures 14 and 15 show the flow patterns in the prototype virtual cyclone at flow rates of 1% and 3% using back-plane particle injection. In Figure 14, 100-Hz illumination is used, whereas double-pulse illumination is used in Figure 15 with the pulse separations shown in the caption. As in Figure 11 with a flow rate of 0.5%, the predicted virtual-cyclone flow pattern is achieved. Since back-plane particle injection is used, the main flow stream has almost no particles in it. In both cases, the virtual cyclone flow patterns are almost identical to Figure 11.

Figures 16-19 show the flow patterns in the prototype virtual cyclone at flow rates of 3%, 10%, 30%, and 90% using mid-plane injection. In Figures 16-18, double-pulse illumination is used, whereas Figure 19 contains video frames and as such uses 100-Hz illumination. Although the main flow stream is more difficult to see due to the presence of particles in it, the eddy in the chamber is clearly visible at all flow rates. Due to an attempt to mask out some of the laser light reflected from the curved wall, this wall is only partially visible, which makes it somewhat harder for the eye to see the main flow stream. Figure 17 shows additional views of the flow pattern at a flow rate of 10%. Due to a film-processing error, these photographs are partially cropped so that the left portion of the virtual cyclone is not visible. These photographs illustrate roll-up of the shear layer (turbulent mixing), which is first observed to occur repeatedly at the 10% flow rate and can be seen without difficulty in the video. Shear-layer roll-up is also observed in the video during the transient flow that exists briefly when changing from one flow rate to another. Without the video, it would be extremely difficult to observe this transient roll-up phenomenon.

Figures 18 and 19 show the flow patterns in the virtual cyclone at flow rates of 30% and 90%. Due to the large flow rates, the flow from the nebulizer is drawn into a thin stream near the middle of the inlet. Although some particle separation is observed, turbulent mixing appears to dominate at these flow rates since shear-layer roll-up is observed almost continually for these cases. Figures 18(b) and 19(b) show different phases of another unusual phenomenon. The large bright spot near the center of Figure 18(b) is a 0.5-cm-diameter water drop adhering to the inner surface of the nearest side disk. This water droplet appears to be held in place by the reduced pressure existing in the core of the eddy. In Figure 19(b), several slightly smaller drops are observed in the middle and the upper left of the frame. In the video, these drops are observed to slide along the side disk surface and swirl around the core of the eddy. As they circle the core, these drops grow in size and ultimately merge into the larger drop shown in Figure 18(b).

(a)

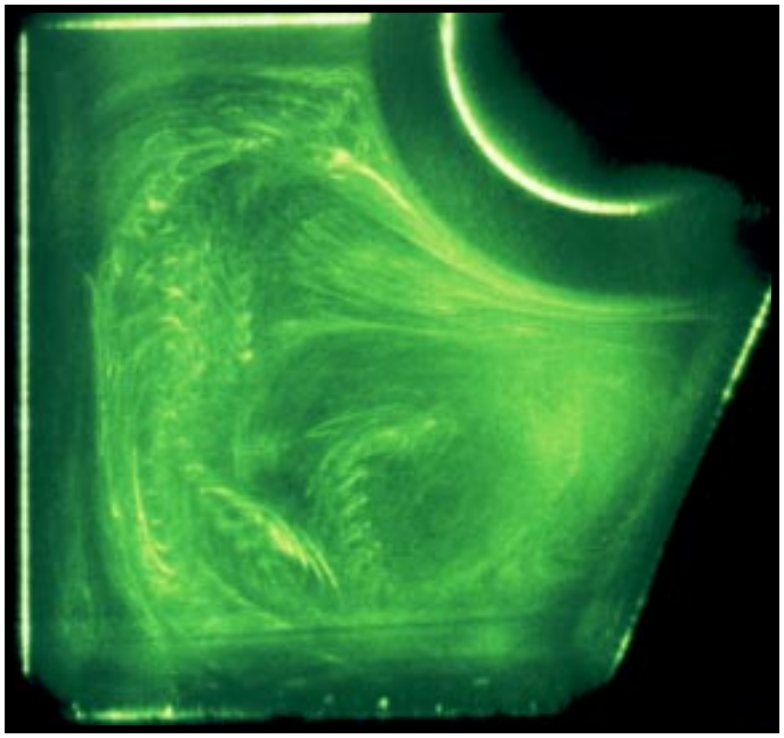

(b)

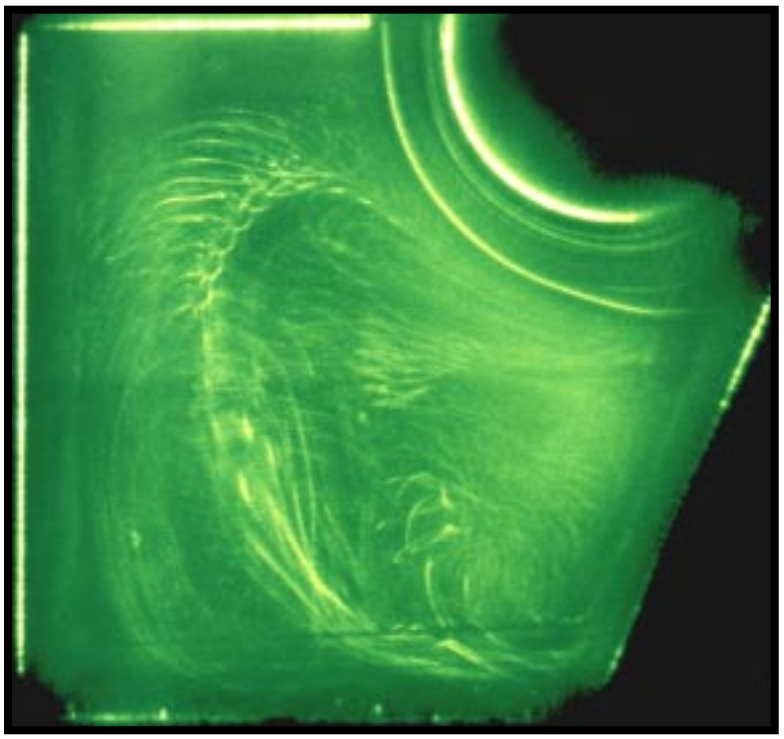

Figure 11. Photographs around 1% with 100 Hz. Smoke: (a) at back; (b) at middle.

(a)

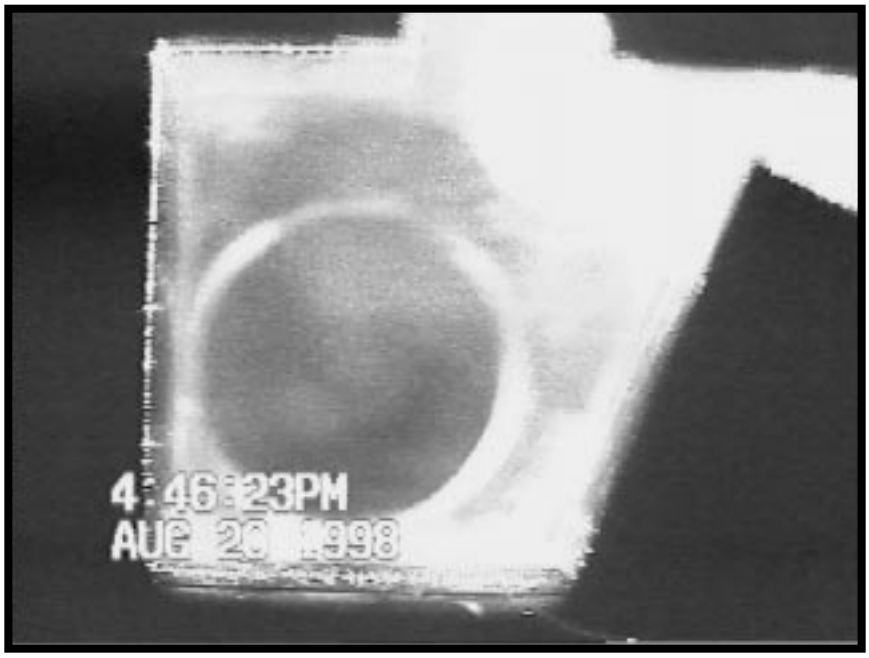

(b)

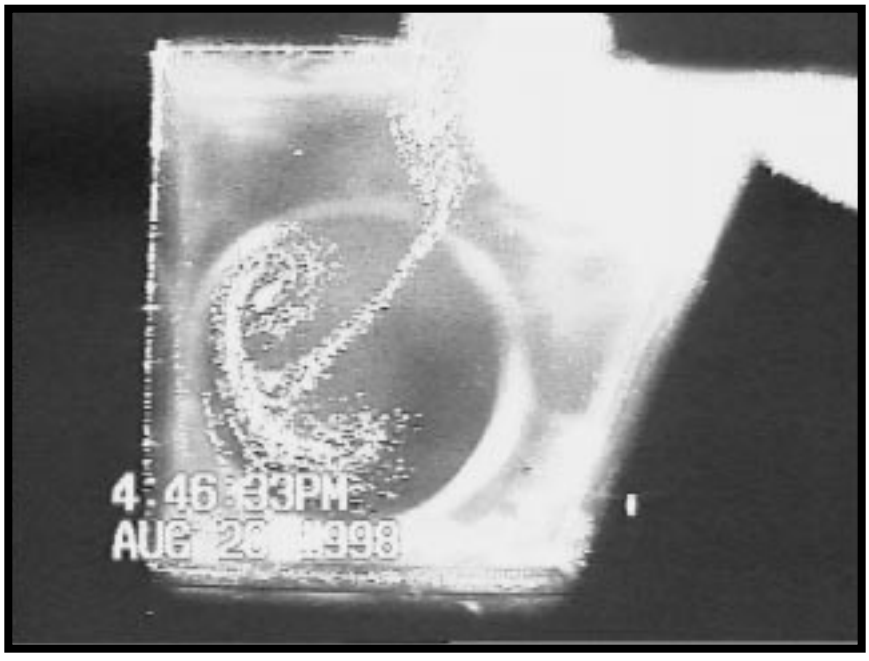

Figure 12. Video at 0% with 100 Hz. Nebulizer: (a) off; (b) on.

(a)

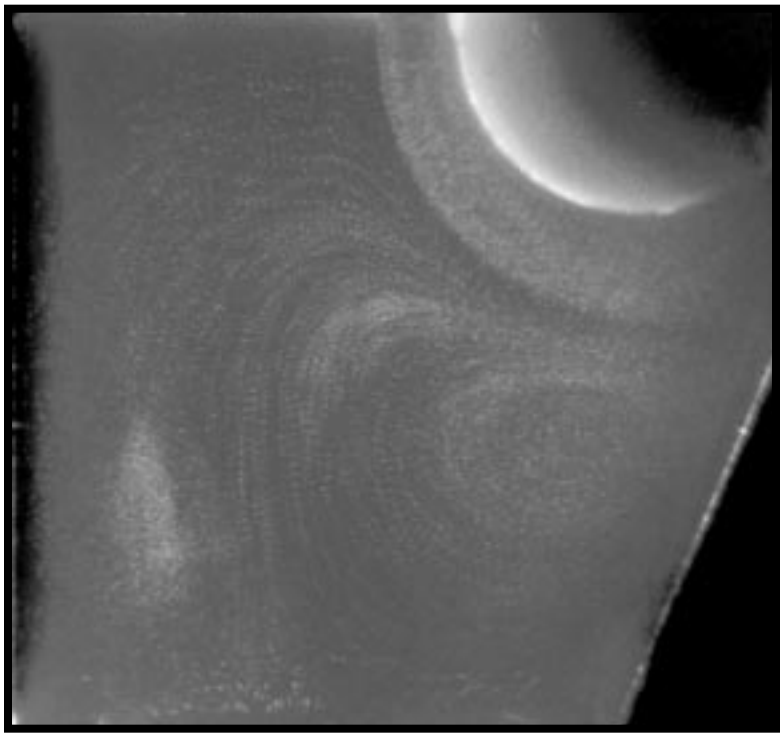

(b)

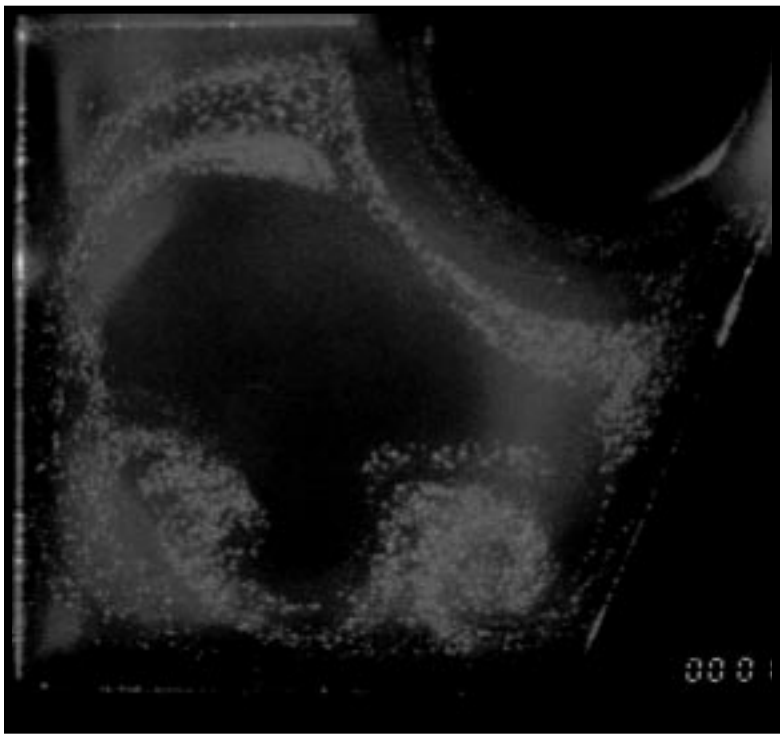

Figure 13. Photographs at 0.5%. Nebulizer at: (a) middle, 100 Hz; (b) back, 20 ms.

(a)

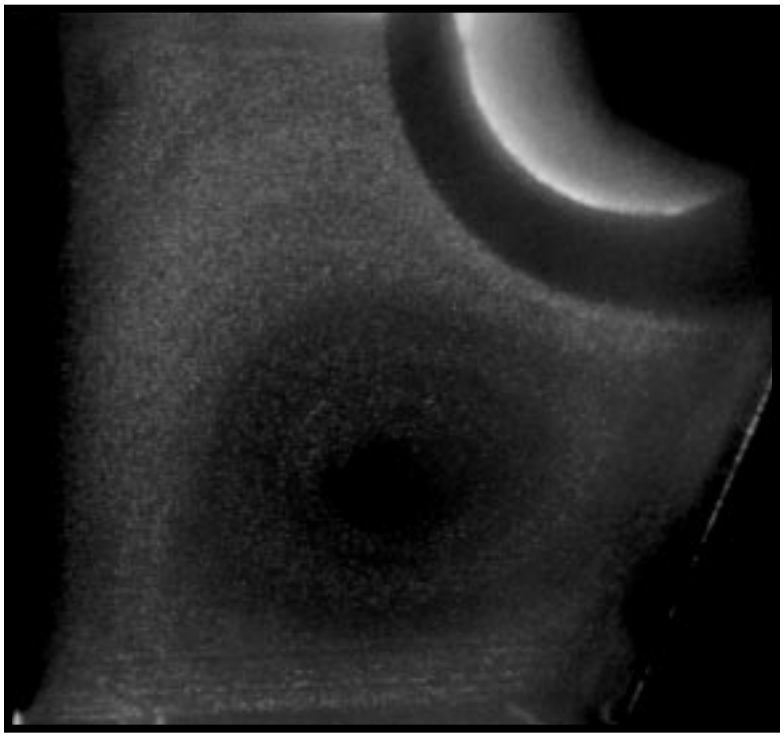

(b)

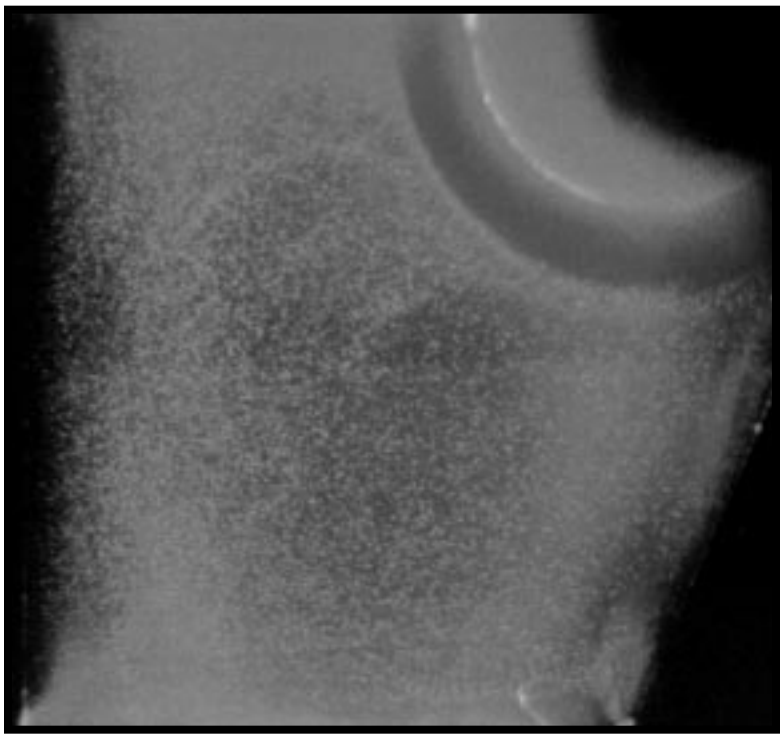

Figure 14. Photographs with nebulizer at back, 100 Hz. Flow at: (a) 1%; (b) 3%.

(a)

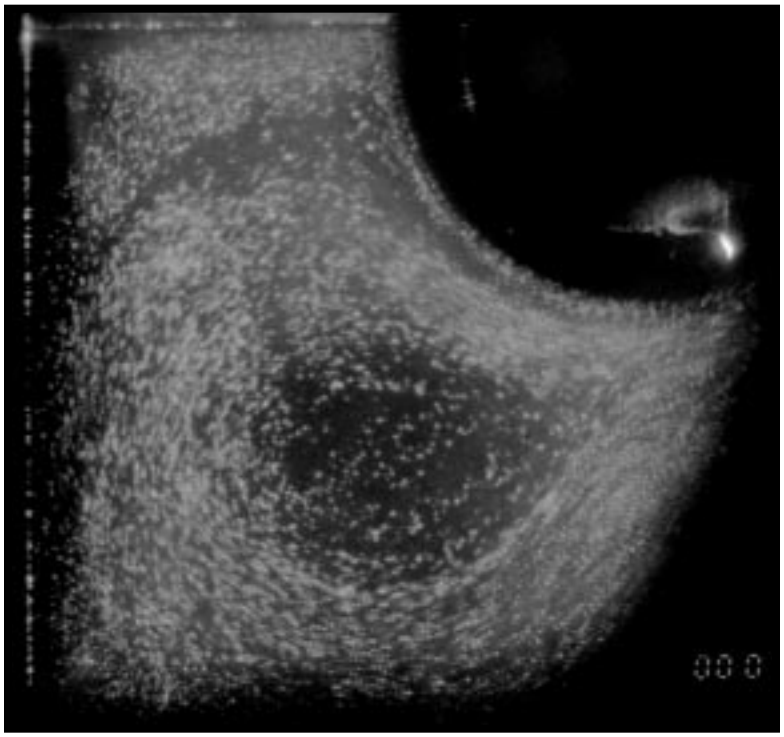

(b)

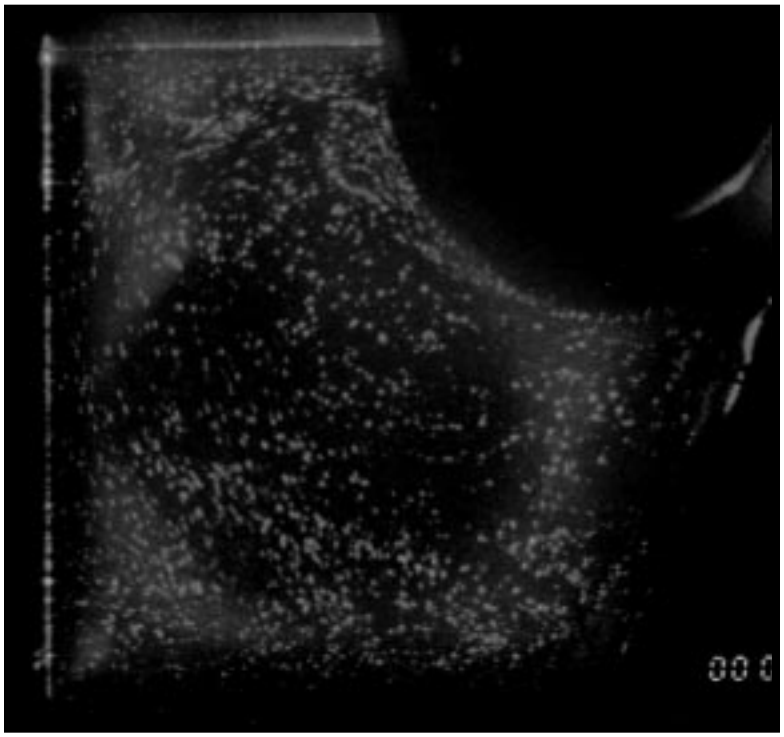

Figure 15. Photographs with nebulizer at back. Flow at: (a) 1%, 1 ms; (b) 3%, 0.5 ms.

(a)

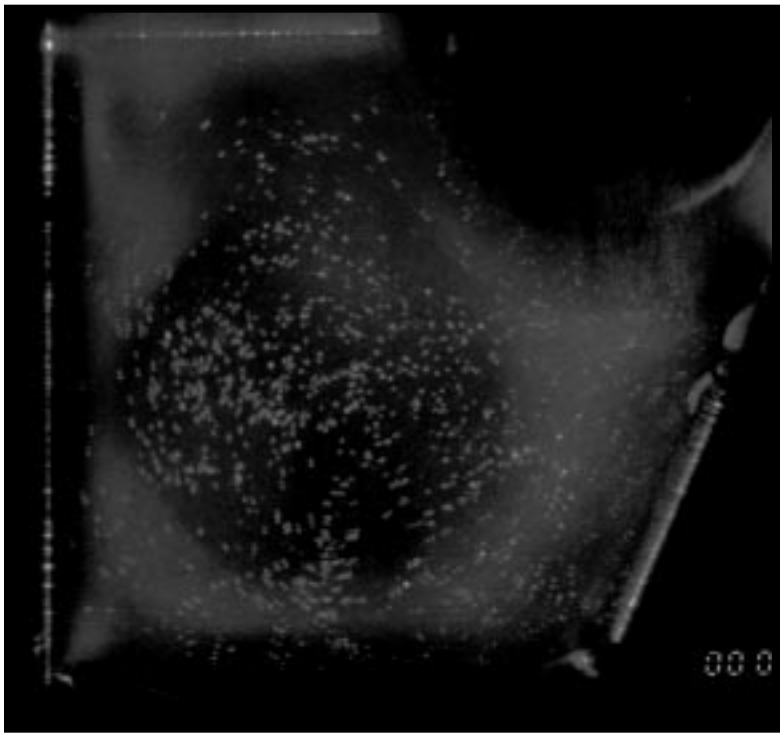

(b)

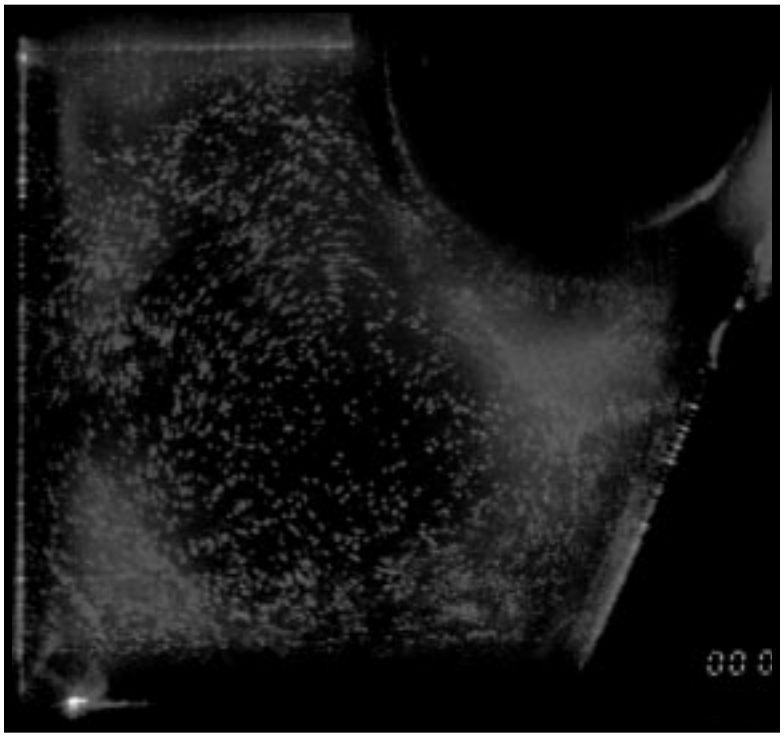

Figure 16. Photographs with nebulizer at middle. Flow at: (a) 3%, 0.5 ms; (b) 10%, 0.1 ms.

(a)

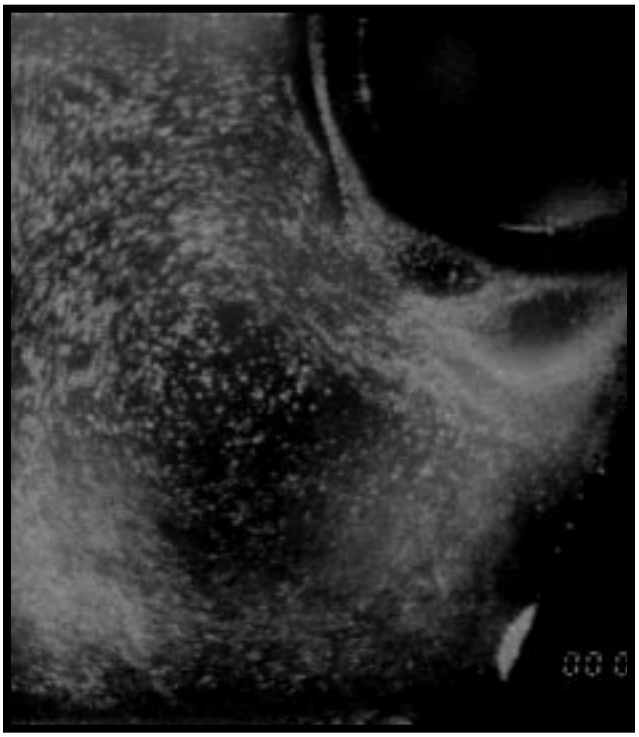

(b)

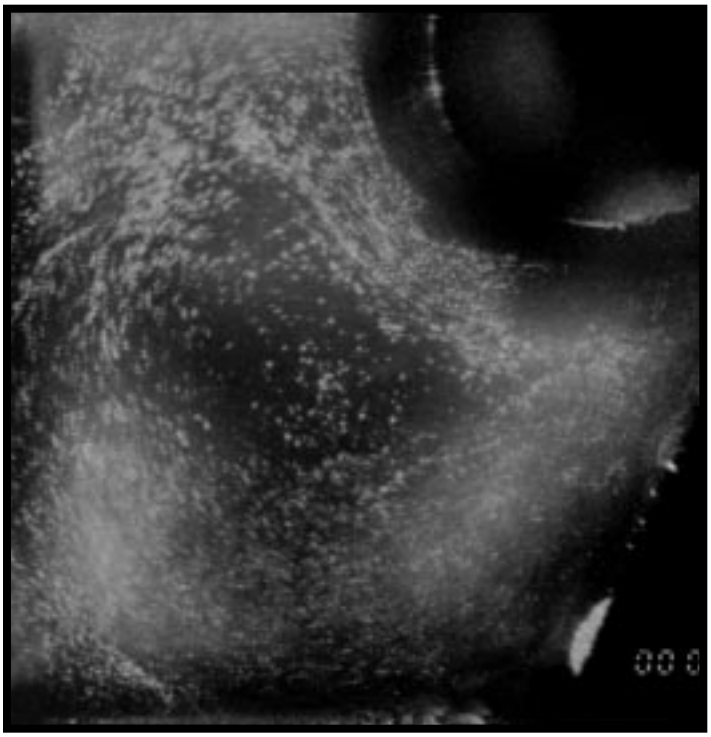

Figure 17. Photographs at 10% with nebulizer at middle, 0.1 ms: (a,b) shear-layer roll-up.

(a)

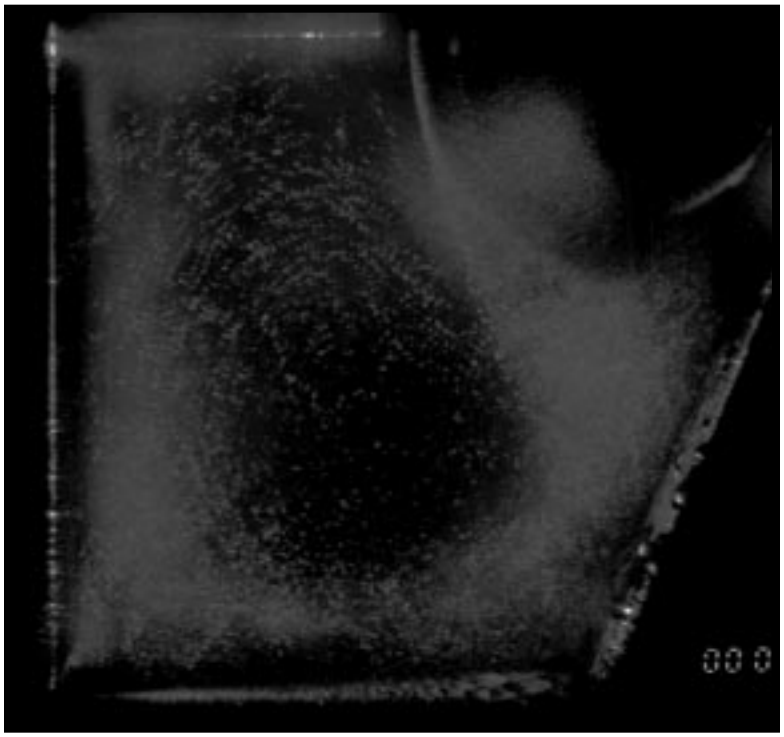

(b)

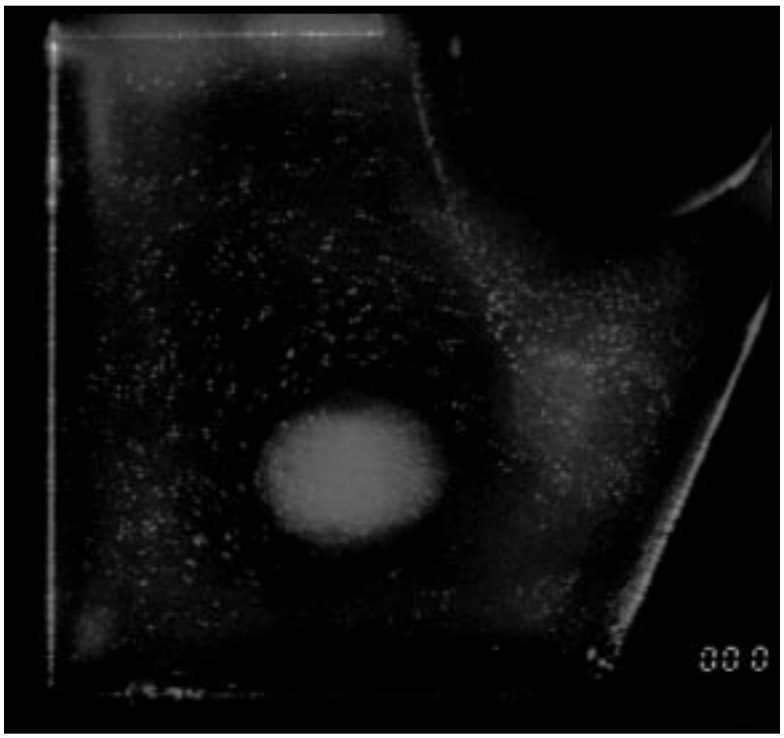

Figure 18. Photographs with nebulizer at middle. Flow at: (a) 30%, 50 µs; (b) 90%, 10 µs.

(a)

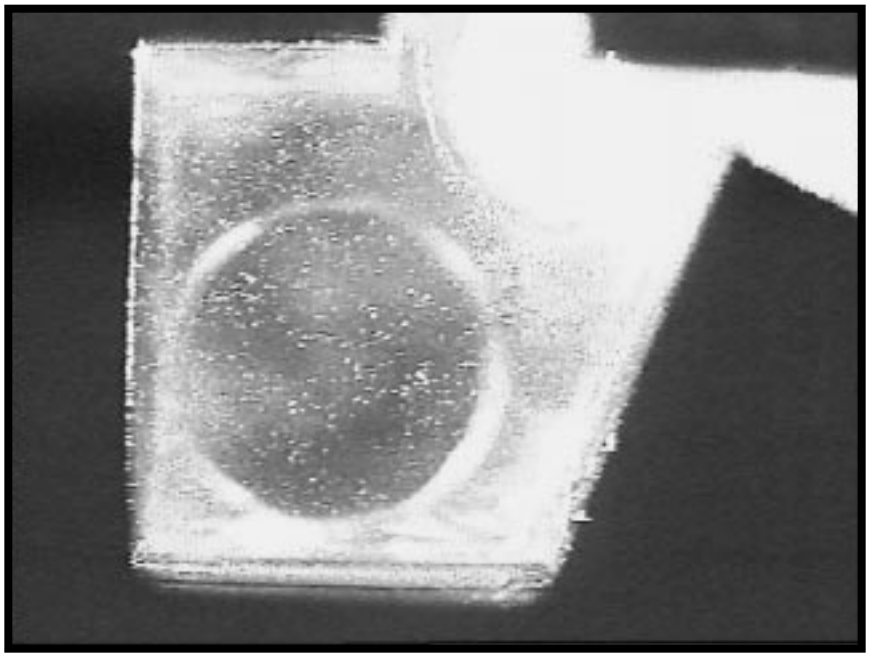

(b)

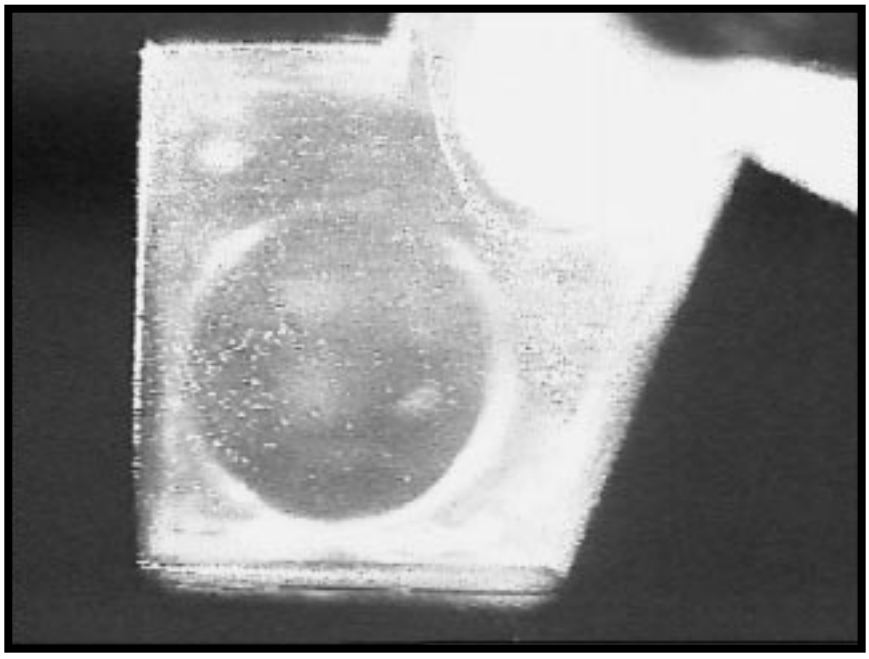

Figure 19. Video with nebulizer at middle and 100 Hz. Flow at: (a) 30%; (b) 90%.

4.4. Particle-Imaging Velocimetry (PIV) Results

The double-pulse photographs presented in the previous section contain the information needed to perform particle-imaging velocimetry (PIV). As previously discussed, the velocity of a particle can be calculated using the difference in position between two correlated particle images and the known temporal separation of the two laser pulses. No systematic PIV analysis has as yet been attempted. However, Figures 15-18 have been analyzed manually to determine the regionally averaged speed U_c within a subarea of the chamber, as indicated in Figure 20. These values are shown in Table 5. The regionally averaged speed is seen to increase monotonically with inlet speed as expected. The speed ratio U_c/U is seen to decrease initially with increasing inlet flow speed, as expected for laminar flow (Torczynski and Rader, 1997). However, this ratio increases sharply at a flow rate of 10% and subsequently increases somewhat with inlet flow speed, as would be expected for turbulent flow (Torczynski and Rader, 1997). This is in harmony with the observation of shear-layer roll-up first occurring at a flow rate of 10%.

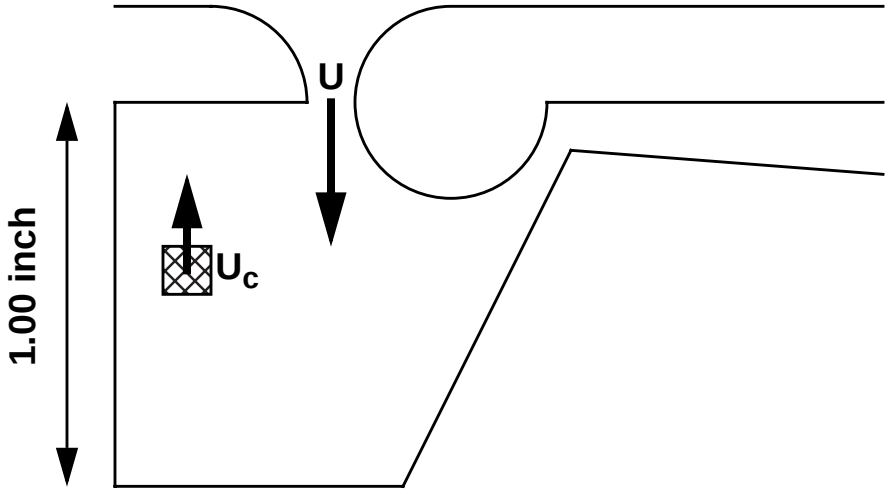

Figure 20. Region (to scale) in which average flow speed is computed by PIV approach.

Table 5. Regionally averaged and inlet flow speeds and their ratio from the PIV approach.

Meter (%)	U_c (m/s)	U (m/s)	U_c/U
1	0.13	1.24	0.10
3	0.30	3.72	0.08
10	1.9	12.4	0.15
30	7.1	37.2	0.19
90	35.	112.	0.31

5. Discussion

The results in the previous section can be summarized as follows. The predicted virtual-cyclone flow pattern is observed at all flow rates and Reynolds numbers. The flow appears to be laminar and steady for Reynolds numbers below a few thousand and turbulent at higher Reynolds numbers based on the observed shear-layer roll-up (turbulent mixing).

The presence of turbulence in the flow limits the potential of the virtual cyclone as a particle concentrator in the following manner. Denote the main flow rate by $\dot{V}$ and the particle concentration in the main flow by c. The maximum possible rate of particle transfer into the chamber is clearly $c\dot{V}$. Turbulence causes an exchange of material between the chamber and the main flow by turbulent mixing. Denote this exchange flow rate from the chamber to the main flow by $\dot{V}_c$ and the particle concentration in the chamber by c_c. So long as particle concentration is conserved, these quantities approximately obey the following relation:

$$c_c \dot{V}_c \approx c(\dot{V} + \dot{V}_c) . \tag{12}$$

This is an inherent limit on the degree to which particle concentration can be increased in the chamber relative to the main flow. If the exchange flow rate is much smaller than the main flow rate, particle concentrations can be increased substantially. If the exchange flow rate is much greater than the main flow rate, then the particle concentration in the chamber is comparable to the particle concentration in the main flow, so essentially no increase is achieved. Turbulence significantly increases the exchange flow rate and, if present, reduces the ability of the virtual cyclone to concentrate particles.

Flow three-dimensionality can have an effect similar to that of turbulence. It is well known that flow over a finite length chamber or cavity can produce three-dimensional motion that directly transports fluid from the main flow into the chamber and vice versa (O'Hern et al., 1997). As a result, flow three-dimensionality produced by finite-length effects increases the exchange flow rate and thereby limits the degree to which particles can be concentrated in a virtual cyclone.

Flow three-dimensionality can be mitigated in at least two possible ways. First, an axisymmetric version of the virtual cyclone could be considered. The resulting flow would be independent of azimuthal angle and therefore have no three-dimensionality. Second, as pointed out by Torczynski and Rader (1996, 1997), use of a large-aspect-ratio inlet (one with $L/H \gg 1$) would greatly reduce the magnitude of any three-dimensionality. In the present study, this ratio has a value of 24. No study has as yet been performed to determine acceptable or optimum values for this parameter.

There are several ways by which the onset of turbulence can be mitigated. Some of these possibilities depend on the cause of the turbulence. If the turbulence in this study is triggered by flow disturbances in the inlet, then turbulent mixing could be reduced substantially by improving inlet conditions. More specifically, an improved inlet design and a "more quiet" inlet flow (less disturbances such as are produced by room ventilation and the particle seeding) would reduce turbulence or increase the Reynolds number at which turbulence first occurs. If the turbulence is triggered by an instability related to an interaction between the chamber geometry and the shear layer, an improved chamber design could stabilize the flow until higher Reynolds numbers. If the turbulence results from the instability of the shear layer alone, some improvement might be gained by controlling the boundary layers upstream of the shear layer. If these approaches are unsuccessful, it is always possible to operate at the highest Reynolds number that achieves steady, laminar flow and separation of the desired particle size.

The scaling properties of the virtual cyclone suggest that fairly small devices offer the possibility of both laminar flow and small particle separation. Torczynski and Rader (1996, 1997) demonstrated that flows with $Re \geq 100$ exhibited the virtual-cyclone flow pattern. In the present study, the onset of turbulence is observed to occur somewhere around $Re \leq 4000$, with steady, laminar flow observed at lower Reynolds number values. Thus, it should be possible to obtain steady, laminar flow and the virtual-cyclone flow pattern by selecting the Reynolds number in the range $100 < Re < 4000$. Recall Equations 1 and 5 for the main flow Reynolds number Re and the efficiency η:

$$Re = \frac{\rho U(2H)}{\mu}, \tag{13}$$

$$\eta \approx \frac{\rho_p D_p^2 U \theta}{18 \mu H}. \tag{14}$$

These relations can be inverted to solve for the inlet flow speed U and the inlet width H:

$$U = \sqrt{\frac{9 \eta Re \mu^2}{\rho_p D_p^2 \rho \theta}}, \tag{15}$$

$$H = \sqrt{\frac{\rho_p D_p^2 \theta Re}{36 \eta \rho}}. \tag{16}$$

If the fluid is air, the particles are 1-μm-diameter water droplets, the turning angle is around $\pi/2$ (it cannot differ significantly from this value), and the efficiency is unity, then the required Reynolds number range of $100 < Re < 4000$ yields the following ranges for the inlet velocity and width: 14 m/s < U < 88 m/s and 66 μm < H < 418 μm. Devices with these scales can probably be fabricated through application of MEMS-related technologies. Since pressure variations within the system scale like $\rho U^2/2$, small-scale systems are also attractive because pressure drops and power requirements are commensurately smaller at constant efficiency.

6. Conclusions

A prototype virtual cyclone has been developed and fabricated, and flow visualization experiments have been performed to examine the flow pattern over a broad range of flow rates. The predicted flow pattern is observed robustly over the entire flow rate range, but the flow becomes turbulent when the Reynolds number of the flow in the inlet exceeds 4000. Turbulent flow adversely impacts the possibility of significantly increasing the particle concentration in the chamber compared to the concentration in the main flow. If turbulence cannot be suppressed for macroscopic-scale virtual cyclones, laminar flow should be achievable for a small-scale (low Reynolds number) virtual cyclone through MEMS-related technologies. This approach could lead to a chip-scale particle concentrator.

Future efforts to refine virtual-cyclone technology should attempt to address the following issues.

1. Turbulence. The cause of the onset of turbulent flow should be identified (e.g., disturbances in the incoming flow, instability of the shear layer, interaction between the shear layer and the eddy). Various methods of turbulence mitigation (e.g., improved inlet geometry, reduction in flow disturbances, different chamber geometry) should be investigated. The degree to which turbulence can be mitigated should be quantified since particle-separation efficiency increases with increasing flow speed in the absence of turbulence.

2. Three-dimensionality. The impact of flow three-dimensionality caused by the finite lateral length should be assessed. The exchange rate of material between the main and eddy flows that results from three-dimensionality should be quantified. The minimum acceptable value of the aspect ratio of the inlet slit (lateral length to width) should be determined. Axisymmetric implementations of the virtual-cyclone concept should be investigated to assess feasibility since they offer the possibility of zero lateral (azimuthal) variation.

3. Optimal inlet design. In all studies performed to date, the ratio of the inlet width to the inner radius has been 0.5. The impact of changing this ratio on flow and particle-separation behavior should be investigated.

4. Optimal chamber design. The chamber used in this study and previous studies has not been optimized. Optimization attempts should examine how the flow and particle-separation behavior is impacted by various geometric parameters (e.g., chamber overall volume, the presence of corners, angles other than 90˚ at the inlet).

5. Flow unsteadiness. The impact of start-up, shut-down, and random flow transients on flow and particle-separation behavior should be quantified.

6. Sampling. The impact of withdrawing some of the fluid from the chamber for sampling purposes while the main flow is ongoing should be assessed.

7. Small-scale fabrication. The possibility of implementing a virtual-cyclone system in a chip-scale concentrator using MEMS-related technologies should be investigated.

References

Fluid Dynamics International, 1993, *FIDAP Users Manual* (versions 7.0, 7.5, and 7.6), Fluid Dynamics International, Evanston, IL.

O'Hern, T. J., Torczynski, J. R., Shagam, R. N., Blanchat, T. K., Chu, T. Y., Tassin-Leger, A. L., and Henderson, J. A., 1997, *Optical Diagnostics for Turbulent and Multiphase Flows: Particle Image Velocimetry and Photorefractive Optics*, Sandia Report SAND94-2589, Sandia National Laboratories, Albuquerque, NM, 100 pages.

Play, Inc., 1998, *Snappy Users Manual* (version 3.0), Play, Inc., Rancho Cordova, CA.

Torczynski, J. R., and Rader, D. J., 1996, *The Anticyclone: A Device for Nonimpact Particle Separation*, Sandia Report SAND96-0728, Sandia National Laboratories, Albuquerque, NM, 31 pages.

Torczynski, J. R., and Rader, D. J., 1997, "The Virtual Cyclone: A Device for Nonimpact Particle Separation," *Aerosol Science and Technology*, Vol. 26, pp. 560-573.

Turton, R., and Levenspiel, O., 1986, "A Short Note on the Drag Correlation for Spheres," *Powder Technology*, Vol. 47, pp. 83-86.

Distribution

MS 1425	1715	D. R. Adkins
MS 9042	8345	D. J. Rader (5)
MS 0151	9000	G. Yonas
MS 0151	9001	A. J. Caldwell
MS 0841	9100	P. J. Hommert
MS 0828	9101	T. C. Bickel
MS 0841	9102	C. M. Hartwig
MS 0826	9111	W. L. Hermina
MS 0826	9111	C. E. Hickox
MS 0834	9112	A. C. Ratzel
MS 0834	9112	T. W. Grasser
MS 0834	9112	T. J. O'Hern (5)
MS 0834	9112	J. R. Torczynski (8)
MS 0835	9113	S. N. Kempka
MS 0827	9114	R. O. Griffith
MS 0827	9114	J. E. Brockmann (5)
MS 0827	9114	A. S. Geller
MS 9018	8940-2	Central Technical Files (1)
MS 0899	4916	Technical Library (2)
MS 0619	12690	Review & Approval Desk (2) For DOE/OSTI

Professor Virgil A. Marple
University of Minnesota
125 Mechanical Engineering
111 Church St. SE
Minneapolis, MN 55455